

A two-fluid model for numerical simulation of shear-dominated suspension flows

Federico Municchi^{a,1}, Pranay P. Nagrani^b, Ivan C. Christov^{a,*}

^a*School of Mechanical Engineering, Purdue University, West Lafayette, Indiana 47907, USA*

^b*National Institute of Technology Karnataka, Surathkal, Mangalore – 575 025, Karnataka, India*

Abstract

Suspension flows are ubiquitous in nature (hemodynamics, subsurface fluid mechanics, etc.) and industrial applications (hydraulic fracturing, CO₂ storage, etc.). However, such flows are notoriously difficult to model due to the variety of fluid-particle and particle-particle interactions that can occur. In this work, we focus on non-Brownian shear-dominated suspensions, where kinetic collisions are negligible and frictional effects play a dominant role. Under these circumstances, irreversible phenomena such as particle diffusion and migration arise, requiring anisotropic stress models to describe the suspension rheology. On a continuum level, reduced-order models such as the suspension balance model (SBM) or the diffusive flux model are commonly used to predict particle migration phenomena. We propose a new method based on the two-fluid model (TFM), where both the phases are considered as interpenetrating continua with their own conservation of mass and momentum equations. Specifically, we show that when an anisotropic stress analogous to that used in the SBM is added to the equilibrium equations for the particle phase, the TFM is able to accurately predict particle migration. Unlike the SBM, the TFM does not require the assumptions of a steady suspension velocity and a Stokesian (inertialess) fluid. Thus, the TFM can be easily extended to include buoyancy and even kinetic collisional models. We present several benchmark simulations of our TFM implementation in OpenFOAM[®], including in curvilinear coordinates and three-dimensional flow. Good agreement between the TFM solutions and previous experimental and numerical results is found.

Keywords: Suspensions, two-fluid model, particle migration, multiphase flow, OpenFOAM

1. Introduction

Non-Brownian suspensions are found in a wide range of applications, ranging from agriculture [10] to hydraulic fracturing [58] and many more. Despite their ubiquitous presence in nature and engineering, understanding and modeling the physics of dense suspensions is still a frontier topic of modern fluid mechanics [55, 9]. In fact, while many problems related to dense granular flows are close to being understood [27, 16], a full tensorial form for the suspension stress, which can be applied to any geometry, is not yet available [22, 37].

1.1. Shear flows of suspensions

Shear-dominated suspensions play a significant role in industrial processes, for example those involving particle separation [56]. This is because of the “peculiar” irreversible phenomena, such as shear-induced particle migration and particle diffusion [29], that arise in the flow of suspensions in this regime. Shear-induced particle migration leads to a net particle flux from regions of high shear rate to regions of low shear rate, and it was believed to originate from long-range hydrodynamic interactions between particles [29], even if recent studies suggest particle collisions also play a role [46]. Such drift has obvious significant consequences in processes involving channel flows, since it tends to focus the particles near the channel’s centerline. The phenomenon of self-diffusion in shear flows of suspensions

* Author to whom correspondence should be addressed.

Email addresses: fmunicch@purdue.edu (Federico Municchi), christov@purdue.edu (Ivan C. Christov)

URL: <https://github.com/fmuni> (Federico Municchi), <http://tmmt-1ab.org> (Ivan C. Christov)

¹ Present address: School of Mathematical Sciences, The University of Nottingham, University Park, Nottingham, NG7 2RD, UK.

was observed experimentally by Leighton and Acrivos [29] and was considered to be caused by the inhomogeneous particle distribution resulting from the migration flux. Their measurements suggested that these displacements alter the apparent suspension viscosity.

For the present study, the typical conditions encountered in shear-dominated suspension flows can be summarized as follows:

- i the particles are large;
- ii the fluid flow is inertialess;
- iii the particle flow is only weakly collisional.

Condition (i) is generally quantitatively assessed by requiring that the particle diameter d_p is larger than $\approx 1 \mu\text{m}$. Physically, this condition means that random fluctuations of the flow field should not affect the particle phase significantly, and that effects of Brownian motion can be neglected.

Condition (ii) requires that the particle Reynolds number Re_p is small:

$$Re_p = \frac{\rho_f U_f d_p}{\mu_f} \ll 1, \quad (1)$$

where ρ_f and μ_f are, respectively, the density and viscosity of the suspending fluid, and U_f is a characteristic fluid velocity. In fact, Han et al. [23] observed that when the particle Reynolds number is increased above a certain threshold ($Re_p \approx 0.2$ for tubes) particle migration is replaced by a different kind of irreversible mechanism: the Segré–Silberberg effect [51]. Furthermore, Picano et al. [48] demonstrated that inertial shear thickening appears in shear-dominated dense particle suspensions. This effect is not accounted for in the rheological models that we consider, and thus we will always require that Re_p is well below the threshold at which these effects are significant.

Condition (iii) requires that the shearing forces, and not the collisional interactions, dominate the suspension mechanics. This condition is made precise by requiring that the Péclet number Pe , representing the ratio between the shearing forces and the collisional density (particle random fluctuations), is sufficiently large (ideally infinite):

$$Pe = \frac{\dot{\gamma} \mu_f}{\rho_f \Theta} \gg 1. \quad (2)$$

Here, $\dot{\gamma}$ is a characteristic suspension shear rate, and Θ is the granular temperature of the particle phase expressed in m^2/s^2 (see [20] for an exhaustive discussion on the definition of the granular temperature). Equation (2) also represents the non-Brownian nature of the suspension, since it implies that the shearing forces are much larger than the forces causing the particles' random fluctuations. Notice that equation (2) does not imply that particles do not collide at all, but that frictional interactions dominate the suspension dynamics.

Energy applications such hydraulic fracturing (see, e.g., [24]) make use of shear-dominated dense suspensions. Specifically, suspensions of particles (termed ‘proppants’) are injected into newly created fractures to increase fracture conductivity and prevent closure of the fracture upon the cessation of flow [59]. The proppant distribution is thus critical in such applications. It has been argued that proppant transport involves precisely a dense suspension flows in the above-described regime of $Re_p \ll 1$ and $Pe \gg 1$ [12]. Two Fluid Models (TFMs) are becoming popular for such applications [12, 13, 53], however, these are often further reduced to simplified sets of equations to allow for their numerical solution. Thus, a general numerical TFM framework that can be used to address proppant transport questions is lacking.

Finally, suspension flows do not have to be restricted the regimes (and conditions) mentioned here. In general, a wide variety of transitional phenomena may occur. Therefore, methods for the numerical simulation of suspension flows should be flexible enough to account for flow with inertial and non-inertial regions, or flows in which kinetic collisions play an important role. We posit that TFMs could pave the way towards such general formulations.

1.2. Numerical simulation of shear-dominated suspensions

A wide range of numerical methods have been used to study the rheology of shear-dominated suspensions, and to predict the macroscopic behaviour of suspension flows. Maxey [33] reviews several discrete methods in which

particles are tracked or accounted for individually. Such methods are generally employed to investigate the suspension rheology, as done by Yeo and Maxey [63], who used the Force Coupling Method (FCM) to calculate normal stress differences of the suspension. However, these methods are too computationally expensive to be employed in the prediction of flows occurring in nature or during industrial processes. Thus, it is necessary to develop continuum models for suspensions.

Typically, these continuum models can be classified into three categories: Diffusive Flux Models (DFMs), Suspension Balance Models (SBMs) and Two Fluid Models (TFMs). DFMs and SBMs are both mixture models, where the suspension is described as a single non-Newtonian fluid (the suspension is seen as a single continuum [22]) whose rheology depends upon the particle volume fraction. These models require the solution of a vector parabolic equation for the mixture velocity and a scalar hyperbolic equation for the particle volume fraction, as well as the Poisson equation for the pressure. In DFM and SBM models, an additional diffusive flux \mathbf{J}_{diff} arises in the advection equation for the particle volume fraction.

To make this distinction more clear, consider the suspension's volume-averaged velocity

$$\mathbf{u}_{\text{mix}} = \phi \mathbf{u}_p + (1 - \phi) \mathbf{u}_f, \quad (3)$$

which is defined as the convex combination of the fluid velocity \mathbf{u}_f and the particle velocity \mathbf{u}_p , with the particle volume fraction ϕ used as the weight. Then, the advection equation for ϕ becomes:

$$\frac{\partial \phi}{\partial t} = -\nabla \cdot (\mathbf{u}_p \phi) = -\nabla \cdot (\mathbf{u}_{\text{mix}} \phi) - \nabla \cdot [(\mathbf{u}_p - \mathbf{u}_{\text{mix}}) \phi] = -\nabla \cdot (\mathbf{u}_{\text{mix}} \phi) - \nabla \cdot \mathbf{J}_{\text{diff}}, \quad (4)$$

having introduced the diffusive flux \mathbf{J}_{diff} as a closure accounting for the *a priori* unknown flux arising due to the term $(\mathbf{u}_p - \mathbf{u}_{\text{mix}}) \phi$. In the DFM [29, 47, 60], this closure is fundamentally a phenomenological one, and the diffusive flux is modeled as:

$$\mathbf{J}_{\text{diff}} = -(D_\phi \nabla \phi + D_\gamma \nabla \dot{\gamma}). \quad (5)$$

Here, D_ϕ and D_γ are diffusion coefficients determined empirically or through experiments. On the other hand, in the SBM [42, 39, 35, 43, 7] the diffusive flux is computed by upscaling the *steady-state* equations of a two fluid model. As result, \mathbf{J}_{diff} is given by the product of the particle mobility M with the divergence of the particle phase stress Σ_p :

$$\mathbf{J}_{\text{diff}} = -M \nabla \cdot \Sigma_p. \quad (6)$$

Vollebregt et al. [60] showed that the DFM and SBM models are equivalent in the case of isotropic particle phase stress, in which case $\nabla \cdot \Sigma_p$ can be expressed as the gradient of a potential μ^* .

1.3. The two fluid model

The latter idea of expressing $\nabla \cdot \Sigma_p$ as the gradient of a potential was recently employed by Drijer et al. [14] to develop a TFM using the computational environment provided in STAR-CCM+. In the TFM, the fluid and particles are modeled as two distinct interpenetrating continua, thus allowing for a more detailed description of the multiphase flow dynamics with respect to mixture models. However, this approach comes at a significant computational cost (compared to DFM and SBM), since two coupled vector equations have to be solved for the phases' velocity fields. In the formulation of Drijer et al. [14], an additional forcing term $\mathbf{F}_{\text{SID}} = -\nabla \mu^*$ is added to the particle momentum equation and subtracted from the fluid momentum equation. In their model, they defined $\nabla \mu^* = (D_\phi \nabla \phi + D_\gamma \nabla \dot{\gamma}) / M$, which makes their model a combination of a DFM and a TFM. However, this model cannot account for the anisotropy of the particle stress tensor, therefore it is not suitable for problems in curvilinear geometries.

It is crucial to note that while SBM and DFM are indeed essentially multiphase models, they require the solution of only one momentum conservation equation for the whole suspension. Therefore, the suspension is modeled as a single fluid whose rheology depends on the scalar field ϕ (the particle volume concentration). Therefore, a total of five coupled equations (three for \mathbf{u}_{mix} , one for the hydrodynamic pressure p , and one for ϕ) have to be solved. By contrast, a TFM requires the solution of the momentum conservation equations for both phases, leading to a total of *eight* coupled equations (three for \mathbf{u}_p , three for \mathbf{u}_f , one for p and one for ϕ). This is a fundamental mathematical, computational and physical difference between the TFM and the SBM/DFM.

The TFM formulation of multiphase flows is very popular in the particulate flow community, since it is able to accurately capture non-equilibrium phenomena, which is an essential feature for developing upscaled models like the filtered TFM [34]. On the other hand, the SBM and DFM formulation are mostly employed in the suspensions community.

1.4. Goals and outline of the paper

In this work, we aim to establish a formulation of the TFM that is valid for shear-dominated suspension flows in general curvilinear geometries and that can be straightforwardly extended to collisional or inertial flows. To this end, we modify the *twoPhaseEulerFoam* solver from the finite volume library OpenFOAM[®] to include the anisotropic particle stress tensor models employed in the SBM. In our TFM formulation, particle migration is not modeled as an additional forcing term, rather it is incorporated in the particle phase stress. The objective is to provide an open-source implementation of a sufficiently general and extensible TFM that can be used for testing future rheological models or for specific applications of suspension flows in the limit of $Pe \gg 1$.

To this end, this paper is structured as follows: in section 2, we describe the governing equations and the rheological models that we employ. Section 3 briefly outlines the numerical implementation of the method, with an emphasis on the anisotropic stress tensor. We demonstrate the accuracy of the proposed computational framework in section 4. In the conclusions (section 5), we discuss further improvements and potential future work. Meanwhile, a grid sensitivity analysis is presented in the appendix.

2. Mathematical formulation

2.1. Governing equations

In the TFM, the continuity and equilibrium equations for the two phases are solved separately. Our formulation follows [45], which is standard for two-phase flow solvers. However, we write the equations in a more compact form, which is useful for non-Brownian suspensions [39, 12]. Introducing the particle volume fraction field $\phi(\mathbf{x}, t)$, we write the governing equations for the two phases [26, 4, 19] as:

$$\frac{\partial}{\partial t} (\rho_p \phi) + \nabla \cdot (\rho_p \mathbf{u}_p \phi) = 0, \quad (7)$$

$$\frac{\partial}{\partial t} [\rho_f (1 - \phi)] + \nabla \cdot [\rho_f \mathbf{u}_f (1 - \phi)] = 0, \quad (8)$$

$$\frac{\partial}{\partial t} (\rho_p \phi \mathbf{u}_p) + \nabla \cdot (\rho_p \phi \mathbf{u}_p \otimes \mathbf{u}_p) = \nabla \cdot \boldsymbol{\Sigma}_p + \phi \rho_p \mathbf{g} + \mathbf{f}_d, \quad (9)$$

$$\frac{\partial}{\partial t} [\rho_f (1 - \phi) \mathbf{u}_f] + \nabla \cdot [\rho_f (1 - \phi) \mathbf{u}_f \otimes \mathbf{u}_f] = -\nabla \cdot (p \mathbf{I} - \boldsymbol{\tau}_f) - \nabla p_p - \mathbf{f}_d + (1 - \phi) \rho_f \mathbf{g}, \quad (10)$$

where the subscript ‘ p ’ refers to a particle-phase quantity, and the subscript ‘ f ’ refers to a fluid-phase quantity; \otimes denotes the (direct) dyadic product. Also, ρ_p and ρ_f are the particle and fluid densities (assumed constant), \mathbf{u}_p and \mathbf{u}_f are the particle and fluid velocity fields, $\boldsymbol{\Sigma}_p$ is the particle-phase stress tensor, $\boldsymbol{\tau}_f$ is the deviatoric stress tensor of the fluid phase, \mathbf{f}_d is the interphase force, and \mathbf{g} is the gravitational acceleration vector. Here, $p = p_f + p_p$ is the ‘shared’ pressure, which satisfies the Poisson equation in the case of an incompressible suspension, and it is given by the sum of the fluid pressure p_f and the particle pressure p_p . Terms such as $\mathbf{u}_f \mathbf{u}_f$ are to be interpreted as dyadic products. Notice that, unlike in the SBM and DFM, we do *not* need to introduce or model the phenomenological quantity \mathbf{J}_{diff} , since we are directly computing the particle phase’s velocity field \mathbf{u}_p .

2.2. Interphase momentum transfer

We write the interphase force \mathbf{f}_d as the combination of a term due to the local distortion of the flow field and a generalized buoyancy. In this form, the interphase force is often referred to as the Clift drag [11]:

$$\mathbf{f}_d = K_d (\mathbf{u}_p - \mathbf{u}_f) + \phi \nabla \cdot (\boldsymbol{\tau}_f - p \mathbf{I}). \quad (11)$$

In this work, we express the drag coefficient K_d as a function of the sedimentation hindrance function $f(\phi)$, which corrects the Stokes sedimentation velocity to account for the presence of neighbouring particles:

$$K_d = \frac{9\mu_f \phi f(\phi)^{-1}}{2d_p^2}. \quad (12)$$

Examples closure expression for $f(\phi)$ will be discussed below [see equations (28) and (29)].

2.3. Rheology of the suspending fluid

We assume the suspending fluid is Newtonian, with a deviatoric stress tensor $\boldsymbol{\tau}_f$ given by

$$\boldsymbol{\tau}_f = 2\mu_f \dot{\boldsymbol{S}}_f, \quad (13)$$

where as before μ_f is the dynamic fluid viscosity (assumed constant), and $\dot{\boldsymbol{S}}_f$ is the shear-rate-of-strain tensor of the fluid phase. For either phase, \boldsymbol{S} is defined based on \boldsymbol{u} as

$$\dot{\boldsymbol{S}} = \frac{1}{2} [\nabla \boldsymbol{u} + (\nabla \boldsymbol{u})^T] - (\nabla \cdot \boldsymbol{u}) \boldsymbol{I}. \quad (14)$$

2.4. Rheology of the suspended phase

The suspended phase's rheology is given by a generalization of the expression in equation (13):

$$\boldsymbol{\Sigma}_p = 2\mu_p \dot{\boldsymbol{S}}_p + \lambda_p (\nabla \cdot \boldsymbol{u}_p) \boldsymbol{I} + \boldsymbol{\Sigma}_s. \quad (15)$$

Here, μ_p and λ_p are the shear and bulk viscosities of the particle phase, respectively. In addition to the classic representation of the stress tensor for a compressible Newtonian fluid, equation (15) contains the extra contribution $\boldsymbol{\Sigma}_s$, which represents the anisotropic stress due to shearing of the solid phase.

In this work, the shear viscosity of the particle phase is further decomposed as

$$\mu_p = \mu_{p,\text{kin}} + \mu_{p,\text{fric}} + \mu_{p,s}, \quad (16)$$

where $\mu_{p,\text{kin}}$ is a kinetic shear viscosity, $\mu_{p,\text{fric}}$ is a frictional shear viscosity, and $\mu_{p,s}$ is the fluid-mediated shear viscosity. The first term in equation (16) is due to the Brownian diffusion of particles, while the second term represents the momentum transfer due to particle contact shearing. The third term is attributed to fluid-mediated interactions between particles in a shear flow. Similarly, we split the particle phase pressure into a kinetic particle pressure $p_{p,\text{kin}}$, arising from the Brownian motion of particles and a frictional component $p_{p,\text{fric}}$, which accounts for force chains emerging at large values of the particle volume fraction:

$$p_p = p_{p,\text{kin}} + p_{p,\text{fric}}. \quad (17)$$

In Brownian suspensions, $\mu_{p,\text{kin}}$, λ_p and $p_{p,\text{kin}}$ are computed following [19] as functions of the granular temperature Θ , which satisfies the transport equation:

$$\frac{3}{2} \left[\frac{\partial}{\partial t} (\phi \rho_p \Theta) + \nabla \cdot (\phi \rho_p \boldsymbol{u}_p \Theta) \right] = (\boldsymbol{\Sigma}_p - p_p \boldsymbol{I}) : \nabla \boldsymbol{u}_p + \nabla \cdot (\kappa_p \nabla \Theta) - \dot{Q}_c + \dot{Q}_\mu + \dot{Q}_s, \quad (18)$$

where κ_p is the granular conductivity and \dot{Q}_c , \dot{Q}_μ and \dot{Q}_s are source terms due to collisions, viscous dissipation and slip velocity. The expressions for these terms employed in OpenFOAM[®] can be found in [30].

However, in the limit of a non-Brownian suspension, the kinetic shear viscosity and the bulk viscosity can be neglected in the definition of $\boldsymbol{\Sigma}_p$, leading to

$$\boldsymbol{\Sigma}_p \sim (\mu_{p,\text{fric}} + \mu_{p,s}) \dot{\boldsymbol{S}}_p + \boldsymbol{\Sigma}_s, \quad Pe \rightarrow \infty. \quad (19)$$

Additionally, the transport equation for Θ plays no role in this limit, therefore it can be neglected, as is generally done in works on non-Brownian suspensions. However, in our OpenFOAM[®] implementation of the TFM that follows, we

retain equation (18) and all the related terms. Doing so allows us (in the future) to employ the proposed TFM to simulate transitional suspension dynamics, i.e., from non-Brownian to Brownian. However, for brevity, such complex flow regimes will not be explored in this work; we focus only on non-Brownian suspensions, leaving the topic of Brownian suspensions for future work.

The anisotropic shear-induced stress tensor Σ_s is generally represented by means of an anisotropy tensor \mathbf{Q} [39], specifically:

$$\Sigma_s = -\mu_f \eta_N(\phi) \dot{\gamma}_{\text{eff}} \mathbf{Q}. \quad (20)$$

Here, η_N is the normal scaled viscosity, and $\dot{\gamma}_{\text{eff}}$ is the effective shear rate defined as

$$\dot{\gamma}_{\text{eff}} = \sqrt{2\dot{\mathbf{S}} : \dot{\mathbf{S}}} + \dot{\gamma}_{\text{NL}}. \quad (21)$$

Here, $\dot{\gamma}_{\text{NL}}$ is the non-local shear rate, which is often employed to ensure $\dot{\gamma}_{\text{eff}} \neq 0$, for example, at the centerline of a channel. The addition of $\dot{\gamma}_{\text{NL}}$ in equation (21) is seen as a way to overcome the breakdown of continuum models when describing phenomena occurring at the particle scale [40, 42, 39, 36]. When such a breakdown occurs, the non-local contribution takes into account the effect of the average stress on a scale on the order of the particle diameter.

An exhaustive description of this phenomenon can be found in [35], where the following expression for $\dot{\gamma}_{\text{NL}}$, valid for channel flows, is proposed:

$$\dot{\gamma}_{\text{NL}} = a_s \frac{u_p^{\text{max}}}{L_{\text{ch}}}. \quad (22)$$

Here, L_{ch} is the characteristic length of the channel, a_s is a model constant, and u_p^{max} is the maximum value of the particle velocity in the channel. Another expression, which does not depend on the flow conditions, was proposed by Gao et al. [18] by fitting a large amount of experimental data:

$$\dot{\gamma}_{\text{NL}} = 0.0176 (\phi_c)^{-2.91}, \quad (23)$$

where ϕ_c is the concentration at the center of the channel, which is unknown *a priori*.

The anisotropy tensor \mathbf{Q} is represented in the classic Cartesian tensor form $\mathbf{Q} = Q^{ij} \mathbf{e}_i \otimes \mathbf{e}_j$ and diagonalized by employing a velocity-field-based coordinate system with orthonormal axes:

$$\mathbf{Q} = \sum_{i=1}^3 \lambda_i(\phi) \mathbf{e}_i \otimes \mathbf{e}_i. \quad (24)$$

Here, $\lambda_i(\phi)$ are the anisotropy weight functions, and \mathbf{e}_i are the unit vectors in the direction of the flow ($i = 1$), gradient ($i = 2$) and vorticity ($i = 3$) of the particle phase velocity. However, while the above definition of the unit vectors is straightforward in unidirectional flows, \mathbf{e}_2 cannot be straightforwardly calculated in general curvilinear three-dimensional flows. Therefore, in this work, we define the unit vectors \mathbf{e}_i as follows:

$$\mathbf{e}_1 = \frac{\mathbf{u}_p}{|\mathbf{u}_p|}, \quad \mathbf{e}_3 = \frac{\nabla \times \mathbf{u}_p}{|\nabla \times \mathbf{u}_p|}, \quad \mathbf{e}_2 = \mathbf{e}_1 \times \mathbf{e}_3, \quad (25)$$

where \times denotes the vector (cross) product. Notice that, by employing equation (25), we calculate an ‘‘implicit’’ gradient direction using the properties of the vector product. Specifically, \mathbf{e}_2 is simply defined as being normal to both the particle velocity field and its curl.

2.5. Closure models for non-Brownian suspensions

In the present work, we incorporate closure models that have been developed for mixture theories (like the SBM or the DFM) into a TFM framework. As discussed in [22], such models describe the overall suspension viscosity and pressure, therefore they do not differentiate between long-range hydrodynamic interaction and frictional contacts. Consequently, such models will be employed to close the particle viscosity μ_p , rather than the frictional viscosity $\mu_{p,\text{fric}}$ or the fluid-mediated shear viscosity $\mu_{p,s}$. Similarly, the effect of the frictional pressure will be absorbed in the

anisotropic stress Σ_s . Notice that a similar approach was employed in [14], where the frictional pressure and viscosity were not included in the governing equations.

Thus, we employ a general expression similar to that proposed in [39] to close the particle phase viscosity:

$$\frac{\mu_p}{\mu_f} = a_\mu + b_\mu \phi \left(1 - \frac{\phi}{\phi_m}\right)^{-1} + c_\mu \left(1 - \frac{\phi}{\phi_m}\right)^{-2}, \quad (26)$$

which returns the closure from [39] for $a_\mu = 0$, $b_\mu = 2.5$ and $c_\mu = 0.1$, and the closure from [32] for $a_\mu = -1$, $b_\mu = 0$ and $c_\mu = 1$. These models have been shown to give the best agreement with experiments when employed within the framework for the SBM [7]. In equation (26), ϕ_m is the maximum allowed particle volume fraction.

For the normal scaled viscosity η_N , we employ the expression proposed in [39]:

$$\eta_N(\phi) = K_N \left(\frac{\phi}{\phi_m}\right)^2 \left(1 - \frac{\phi}{\phi_m}\right)^{-2}, \quad (27)$$

where K_N is usually set to 0.75. Equation (27) also returns the model proposed in [8] for $K_N = 1.08$, and the one proposed in [3] for $K_N = 1$.

The sedimentation hindrance function $f(\phi)$ is modeled using the expression provided in [35]:

$$f(\phi) = \left(1 - \frac{\phi}{\phi_m}\right) (1 - \phi)^{\alpha-1}, \quad \alpha \in [2, 5]. \quad (28)$$

This expression was chosen to ensure that particle migration becomes weaker as $\phi \rightarrow \phi_m$. Another expression often employed can be found in [39]:

$$f(\phi) = (1 - \phi)^\alpha, \quad \alpha \in [2, 5]. \quad (29)$$

Finally, several expressions for λ_i have been proposed in the literature [8, 3, 35]. Taking each to be a particular constant is a common choice, but [8] also proposed volume-fraction-dependent expressions:

$$\lambda_1(\phi) = 1, \quad \lambda_2(\phi) = 0.81 \frac{\phi}{\phi_m} + 0.66, \quad \lambda_3(\phi) = -0.0088 \frac{\phi}{\phi_m} + 0.54. \quad (30)$$

3. Numerical formulation

The governing equations (7)–(10) are solved in a coupled manner using a modified version of the *twoPhaseEulerFoam* solver [45] in OpenFOAM® [61], an open-source library designed for implementing finite volume methods [41]. Momentum predictors are obtained employing the partial elimination algorithm [45], which allow us to decouple the phase momentum equations. In this work, we extend *twoPhaseEulerFoam* to include models for shear-induced migration and to employ the anisotropic stress tensor in place of the frictional pressure. In fact, the main idea behind the approach used in OpenFOAM® is to include the effect of the particle pressure in the suspended (dispersed) phase's continuity equation in an implicit manner.

3.1. Discretized momentum equations

In order to clearly illustrate our modifications to the original algorithm described in [45], below we consider an incompressible suspension in which the phases have constant and equal density (therefore, we drop the gravitational force). Under these assumptions, we can write the semi-discrete momentum equations as

$$\mathbb{A}_p \mathbf{u}_p = \mathbb{H}_p - \mu_f \nabla \cdot (\eta_N \dot{\gamma}_{\text{eff}} \mathbf{Q}) - \phi \nabla p + K_d (\mathbf{u}_p - \mathbf{u}_f), \quad (31)$$

$$\mathbb{A}_f \mathbf{u}_f = \mathbb{H}_f - (1 - \phi) \nabla p + K_d (\mathbf{u}_p + \mathbf{u}_f), \quad (32)$$

where the matrices \mathbb{A}_p and \mathbb{A}_f are the diagonals of the matrices \mathbb{M}_f and \mathbb{M}_p arising from the discretization of the respective momentum equations, with the exception of the undiscrretized terms retained in equations (31) and (32). Meanwhile, the vectors \mathbb{H}_p and \mathbb{H}_f are given by:

$$\mathbb{H}_p = (\mathbb{A}_p - \mathbb{M}_p)\mathbf{u}_p + \mathbb{Q}_p, \quad \mathbb{H}_f = (\mathbb{A}_f - \mathbb{M}_f)\mathbf{u}_f + \mathbb{Q}_f, \quad (33)$$

where \mathbb{Q}_p and \mathbb{Q}_f are the source terms arising from the discretization of the momentum equations (volumetric sources, face-tangential corrections, etc.).

The key idea of the algorithm is to split the anisotropic stress tensor flux in two contributions: one due to the flux arising from a gradient in the particle volume fraction and one due to the flux arising from a gradient in the shear rate or the anisotropy tensor. Specifically,

$$\nabla \cdot (\eta_N \dot{\gamma}_{\text{eff}} \mathbf{Q}) = \dot{\gamma}_{\text{eff}} \left(\frac{d\eta_N}{d\phi} \right) \nabla \phi \cdot \mathbf{Q} + \eta_N \nabla \cdot (\dot{\gamma}_{\text{eff}} \mathbf{Q}). \quad (34)$$

This idea is similar to the diffusive flux model [60, 47], wherein the forcing terms due to the shear-induced migration are written as the gradient of a chemical potential. However, in the present model, we employ a tensor potential instead of a scalar potential. The rightmost term in the decomposition in equation (34) is then subtracted from the vector \mathbb{H} , so that equation (31) becomes:

$$\mathbb{A}_p \mathbf{u}_p = \mathbb{H}_p^* - \dot{\gamma}_{\text{eff}} \left(\frac{d\eta_N}{d\phi} \right) \nabla \phi \cdot \mathbf{Q}, \quad \mathbb{H}_p^* = \mathbb{H}_p - \eta_N \nabla \cdot (\dot{\gamma}_{\text{eff}} \mathbf{Q}). \quad (35)$$

3.2. Pressure equation

The incompressibility condition on the suspension requires surface integrals of the volumetric flux to be zero in every cell. In other words, the total volumetric flux φ must be such that the mixture velocity field \mathbf{u}_{mix} defined in equation (3) is divergence free:

$$\nabla \cdot \mathbf{u}_{\text{mix}} = \nabla \cdot (\phi \mathbf{u}_p) + \nabla \cdot ((1 - \phi) \mathbf{u}_f) = 0, \quad (36)$$

In the finite volume method, equation (36) is satisfied if the sum of the phase volumetric fluxes vanishes in each cell c , i.e.,

$$\int_{\mathcal{V}_c} \nabla \cdot [\phi \mathbf{u}_p + (1 - \phi) \mathbf{u}_f] d\mathcal{V}_c = \sum_{N_{\text{cf}}} \oint_{S_{\text{cf}}} [\phi \mathbf{u}_p + (1 - \phi) \mathbf{u}_f] \cdot d\mathbf{A}_{\text{cf}} = \sum_{N_{\text{cf}}} [\phi_{\text{cf}} \varphi_p + (1 - \phi)_{\text{cf}} \varphi_f], \quad (37)$$

where \mathcal{V}_c is the volume of cell c , \mathbf{A}_{cf} is the area normal to face cf , N_{cf} is the number of faces of cell c , and ϕ_{cf} is the particle volume fraction interpolated at face cf . Additionally, in equation (37), we introduced the volumetric fluxes of the particle phase φ_p and the fluid phase φ_f :

$$\varphi_p = \oint_{S_{\text{cf}}} \mathbf{u}_p \cdot d\mathbf{A}_{\text{cf}}, \quad \varphi_f = \oint_{S_{\text{cf}}} \mathbf{u}_f \cdot d\mathbf{A}_{\text{cf}}. \quad (38)$$

Notice that the phase fluxes are ‘scalar fields’ defined at cell faces rather than at cell centers.

Next, decoupled equations for \mathbf{u}_p are obtained by substituting equation (32) into equation (9). The same approach is employed to obtain decoupled equations for \mathbf{u}_f . Therefore, the volumetric phase fluxes can be expressed as [45]:

$$\varphi_p = \frac{\mathbf{A}_{\text{cf}}}{\zeta_p} \cdot \left[(\mathbb{H}_p^* + K_d \beta_f \mathbb{H}_f)_{\text{cf}} - (\phi + K_d \beta_f (1 - \phi))_{\text{cf}} (\nabla p)_{\text{cf}} - \left(\dot{\gamma}_{\text{eff}} \frac{d\eta_N}{d\phi} \nabla \phi \cdot \mathbf{Q} \right)_{\text{cf}} \right], \quad (39)$$

$$\varphi_f = \frac{\mathbf{A}_{\text{cf}}}{\zeta_f} \cdot \left[(\mathbb{H}_f^* + K_d \beta_p \mathbb{H}_p)_{\text{cf}} - ((1 - \phi) + K_d \beta_p \phi)_{\text{cf}} (\nabla p)_{\text{cf}} + \left(K_d \beta_p \dot{\gamma}_{\text{eff}} \frac{d\eta_N}{d\phi} \nabla \phi \cdot \mathbf{Q} \right)_{\text{cf}} \right], \quad (40)$$

where the subscript ‘cf’ indicates interpolation at cell faces, and

$$\beta_p = \frac{1}{\mathbb{A}_p + K_d}, \quad \beta_f = \frac{1}{\mathbb{A}_f + K_d}, \quad \zeta_p = \mathbb{A}_p - \beta_p K_d^2 + K_d, \quad \zeta_f = \mathbb{A}_f - \beta_f K_d^2 + K_d. \quad (41)$$

Notice that unlike [45], our flux equations (39) and (40) do not have a term of the kind $\mathbf{A}_{cf} \cdot (\nabla\phi)_{cf}$ because we are employing an *anisotropic* stress tensor rather than an isotropic particle pressure. At this stage, this distinction does not constitute a significant computational difference since the term is not updated within the pressure corrector.

The pressure equation is obtained by substituting equations (39) and (40) into equation (36). After solving for p , the new pressure field is used in equations (39) and (40) to update the phase fluxes.

3.3. Continuity equation for the suspended phase

The numerical approach employed has a major impact on the overall algorithm's stability, especially when the particle volume fraction approaches the close-packing limit. To this end, consider the semi-discretized continuity equation for the suspended (dispersed) phase:

$$\frac{\partial\phi}{\partial t} + \nabla \cdot (\phi_{cf}\varphi_s^*) - \nabla \cdot \left[\frac{\phi_{cf}\mathbf{A}_{cf}}{\zeta_p} \cdot \left(\dot{\gamma}_{eff} \frac{d\eta_N}{d\phi} \nabla\phi \cdot \mathbf{Q} \right)_{cf} \right] = 0, \quad (42)$$

where φ_s^* is the volumetric flux of the particle phase φ_p from equation (39) with the contribution from the anisotropic tensor split from it. Notice that the divergence in equation (42) is a semi-discretized operator that acts on face-interpolated scalar fields, and it should be interpreted as a sum over cell faces following a domain discretization. Since $d\eta_N/d\phi$ increases dramatically close to the maximum packing fraction [22], in the standard *twoPhaseEulerFoam* the equivalent rightmost term on the left-hand side of equation (42) is discretized implicitly to avoid instabilities in this regime. However, in the present context, the term cannot be immediately discretized as is because it does not involve just $\mathbf{A}_{cf} \cdot (\nabla\phi)_{cf}$, which can be discretized using standard divergence schemes like upwind, but it involves the double scalar product $\mathbf{A}_{cf} \cdot (\nabla\phi \cdot \mathbf{Q})_{cf}$ instead. Thus, this term requires more than just discretizing the face normal gradient.

To overcome this difficulty, and extract new terms from equation (42) that can be discretized implicitly in time, we decompose the anisotropy tensor into its hydrostatic and deviatoric components:

$$\mathbf{Q} = (\text{tr}\mathbf{Q})\mathbf{I} + \mathbf{Q}_{dev}, \quad \mathbf{Q}_{dev} = \mathbf{Q} - (\text{tr}\mathbf{Q})\mathbf{I}, \quad (43)$$

where $\text{tr}\mathbf{Q} = \sum_{i=1}^3 \mathbf{Q}_{ii}$ is the trace of \mathbf{Q} . Therefore, equation (42) can be rewritten (still considering our semi-discretized definition of the divergence operator) as:

$$\frac{\partial\phi}{\partial t} + \nabla \cdot (\phi_{cf}\varphi_s^*) - \nabla \cdot \left[\left(\dot{\gamma}_{eff} \frac{d\eta_N}{d\phi} \text{tr}\mathbf{Q} \right)_{cf} \frac{\mathbf{A}_{cf}}{\zeta_p} \cdot (\nabla\phi)_{cf} \right] = \nabla \cdot \left[\frac{\phi_{cf}\mathbf{A}_{cf}}{\zeta_p} \cdot \left(\dot{\gamma}_{eff} \frac{d\eta_N}{d\phi} \nabla\phi \cdot \mathbf{Q}_{dev} \right)_{cf} \right]. \quad (44)$$

Notice that now only the term on the right-hand-side of equation (44) can not be discretized implicitly. The approach used in OpenFOAM[®] for solving equation (44) consists of solving the advection equation $\partial\phi/\partial t + \nabla \cdot (\phi_{cf}\varphi_s^*) = 0$ explicitly using the MULES (Multidimensional Universal Limiter for Explicit Solutions) scheme, which is based on the Flux-Corrected Transport (FCT) framework [64, 2]. The remaining terms are solved implicitly in time. External iterations with relaxation are still required to update the last term in equation (44) and obtain an accurate and stable solution. However, their number and the value of the relaxation coefficient are now controlled only by the deviatoric part of \mathbf{Q} .

As a remark, it should be pointed out that equation (44) is parabolic, while the original continuity equation was hyperbolic. This change of type may be an issue, especially regarding the choice of appropriate boundary conditions for ϕ . Therefore, in order to preserve the hyperbolicity of the continuity equation, an implicit formulation of the anisotropic stress should be employed only when facing severe stability issues.

3.4. Numerical solution strategy: Description of the scheme

The solver employs a *PIMPLE* algorithm, which consists of a *PISO* [15] pressure corrector together with external fixed point iterations to couple the phase momentum equations and the continuity equation for the particle phase, as depicted schematically in figure 1. The solver employs a dynamic time stepping based on the Courant number:

$$Co = \frac{\varphi_{Co}\Delta t}{V}, \quad \varphi_{Co} = \max \left(\sum_{cf} \varphi_f, \sum_{cf} (\varphi_f - \varphi_p) \right), \quad (45)$$

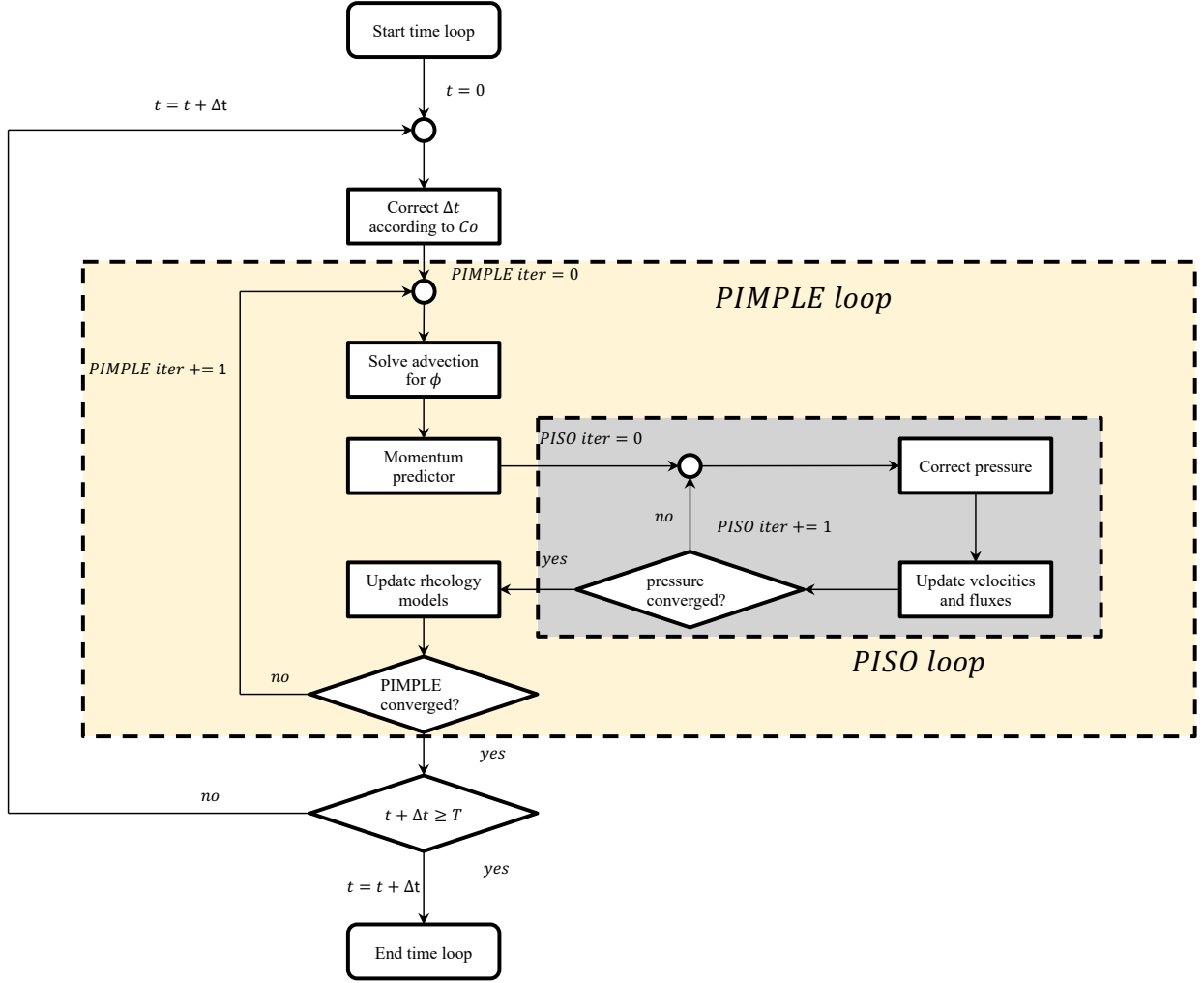


Figure 1: Flowchart illustrating the solution algorithm composed by external iterations (*PIMPLE* loop) and pressure correction iterations (*PISO* loop). Here T is the fixed end time of the simulation. Notice that this is the same algorithm employed in *twoPhaseEulerFoam*.

where Δt is the time step and V is the cell volume field. Notice that the velocity field employed in the definition of C_0 is the maximum between the total suspension flux and the total relative flux in each cell.

The convergence criteria for both the external *PIMPLE* iterations and the *PISO* correctors can be based on the residuals or the number of iterations. In this work, we always limited the number of iterations and set the minimum number of linear solver iterations to one. This choice was made to control residual oscillations and prevent the solver from leaving the loops too early.

3.5. Boundary conditions

Generally, no-slip and no penetration boundary conditions are employed to model walls bounding the flows of non-Brownian suspensions (see, e.g., [8]). The no penetration boundary condition is implemented in OpenFOAM[®] as a *slip* boundary condition, which is fundamentally a symmetric boundary condition that implies no flux normal to the boundary. Such a boundary condition imposes:

$$\mathbf{J}_\phi \cdot \mathbf{n} = 0, \quad \text{with} \quad \mathbf{J}_\phi = \mathbf{u}_s \phi, \quad (46)$$

where \mathbf{n} is the normal vector to the boundary.

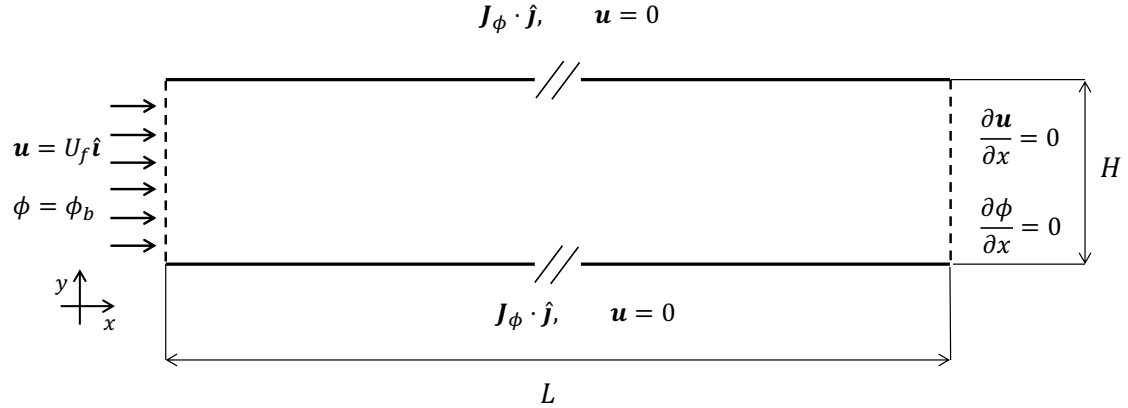


Figure 2: Schematic representation of the two-dimensional (2D) channel geometry, indicating the boundary conditions for the velocity field (both the particle and fluid velocity are represented by a single symbol \mathbf{u}) and the particle phase's volumetric concentration field ϕ . Here, \hat{i} and \hat{j} are the unit normal vector in the x -direction and y -direction respectively, and U_f is the fluid velocity in the particle-based Reynolds number in equation (1), such that $Re_p \approx 10^{-3}$ in this case.

4. Testing and validation

4.1. Planar Poiseuille flow of a suspension

We apply the proposed TFM numerical formulation to the problem of suspension flow between two infinite parallel plates. This problem has been extensively studied in many experimental works [28, 31, 52, 25, 18], which consistently observed a particle flux towards the center of the channel and, thus, an inhomogeneous particle distribution. However, it was argued that the laser-Doppler velocimetry methodology employed by Lyon and Leal [31] significantly underestimates the particle volume concentration near the walls [39]. Recently, Drijer et al. [14] performed an experiment employing a fast confocal microscope (as in [52]) and were able to match the concentration profile with results from their 'hybrid' SBM-TFM simulations in STAR-CCM+. We employ a conduit identical to that used by Dbouk et al. [7], with a ratio between channel height and particle diameter of $H/d_p = 18$. A schematic of the channel geometry and notation is shown in figure 2.

The channel length L is chosen to satisfy the condition for a fully developed concentration profile [42]:

$$\frac{L}{H} \geq \frac{1}{6g(\phi_b)} \left(\frac{H}{d_p} \right)^2. \quad (47)$$

The function $g(\phi_b)$ represents the dependence of the shear-induced diffusion on the bulk (average) particle concentration. This function is generally taken to be (see [29]):

$$g(\phi_b) = \frac{1}{3} \phi_b^2 \left(1 + \frac{1}{2} e^{8.8\phi_b} \right). \quad (48)$$

Notice that, in fully periodic domains, the condition in equation (47) gives the minimum time required to achieve a fully developed concentration profile. In order to drive the flow through the fully periodic channel, a body force is applied that ensures an average value U_f of the fluid (or particle) velocity field. This value is chosen such that the resulting particle Reynolds number [defined in equation (1)] is small, i.e., $Re_p \ll 1$. Then, the condition in equation (47) can be re-expressed as:

$$t \geq \frac{H}{U_f} \frac{1}{6g(\phi_b)} \left(\frac{H}{d_p} \right)^2. \quad (49)$$

We study particles with a diameter $d_p = 50 \mu\text{m}$ suspended in a fluid with $\mu_f = 0.48 \text{ Pa s}$ and $\rho_f = \rho_p = 1.19 \text{ g cm}^{-3}$. We employ the rheological closures suggested by Miller and Morris [35], since those were shown to

produce the most accurate results [7]. The mesh consists of 20 cells in the direction of the gap. For the case of the full channel, the mesh in the flow direction is made of 100 cells with a growth factor of 50 as in [7]. Closures adopted are detailed in table 1. As shown in figure 3, our two-fluid model (TFM) is able to accurately reproduce results from the suspension balance model (SBM).

closure	expression	coefficients
$f(\phi)$	equation (28)	$\alpha = 4$
$\eta_N(\phi)$	equation (27)	$K_N = 0.75$
μ_p/μ_f	equation (26)	$a_\mu = -1, b_\mu = 0, c_\mu = 1$
$\lambda_i(\phi)$	constant values	{1.0, 0.8, 0.5}
ϕ_m	constant value	0.68
$\dot{\gamma}_{NL}$	equation (22)	$a_s = d_p/H$

Table 1: Closure models and parameters used for the parallel plates (planar Poiseuille) configuration.

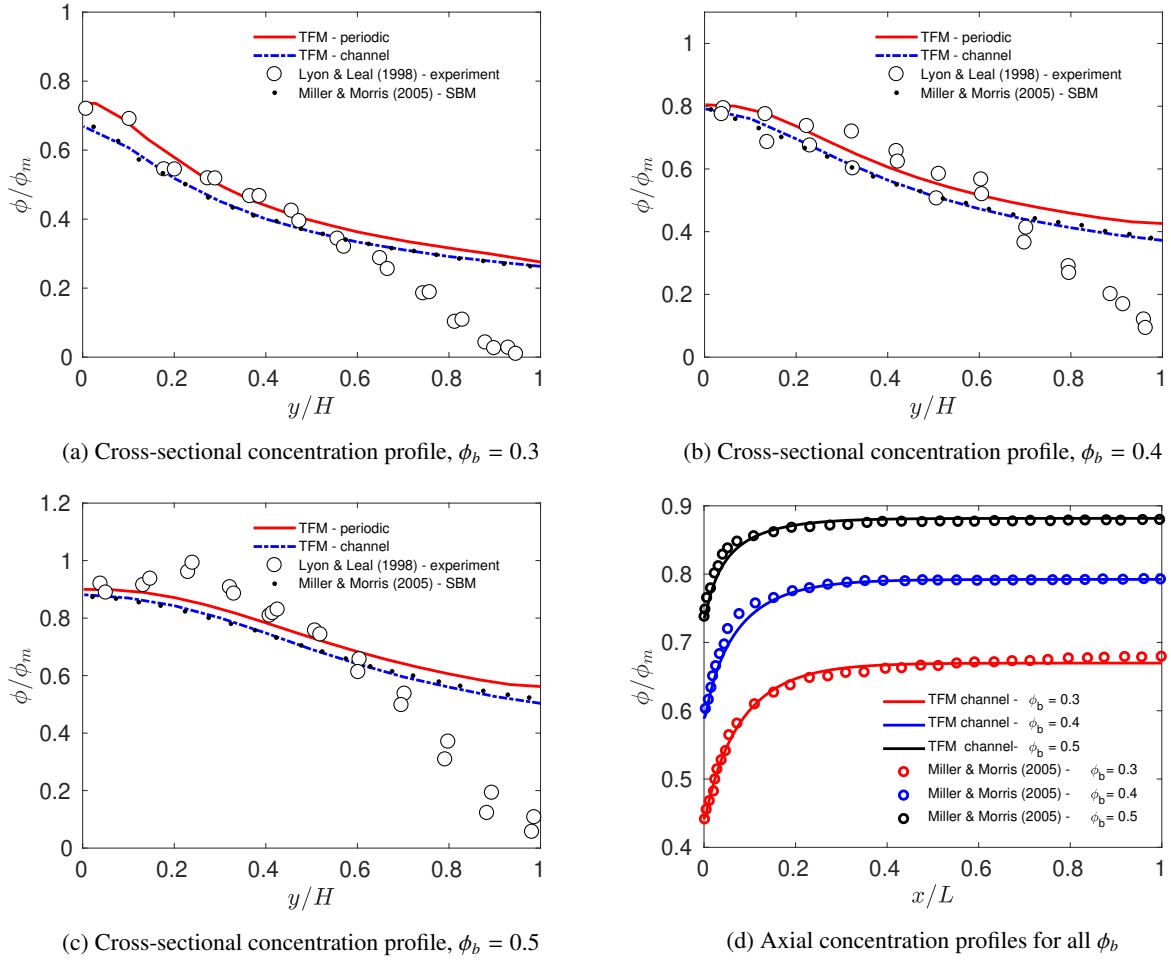


Figure 3: Results for the 2D pressure-driven channel flow from our TFM implementation compared against experimental results from Lyon and Leal [31] and the suspension balance model results of Miller and Morris [35].

Unlike previous computational studies [62, 8, 52], we compare the results obtained with a periodic 2D domain to those obtained with an entire channel domain. Figure 3 shows that a difference exists between the two configurations,

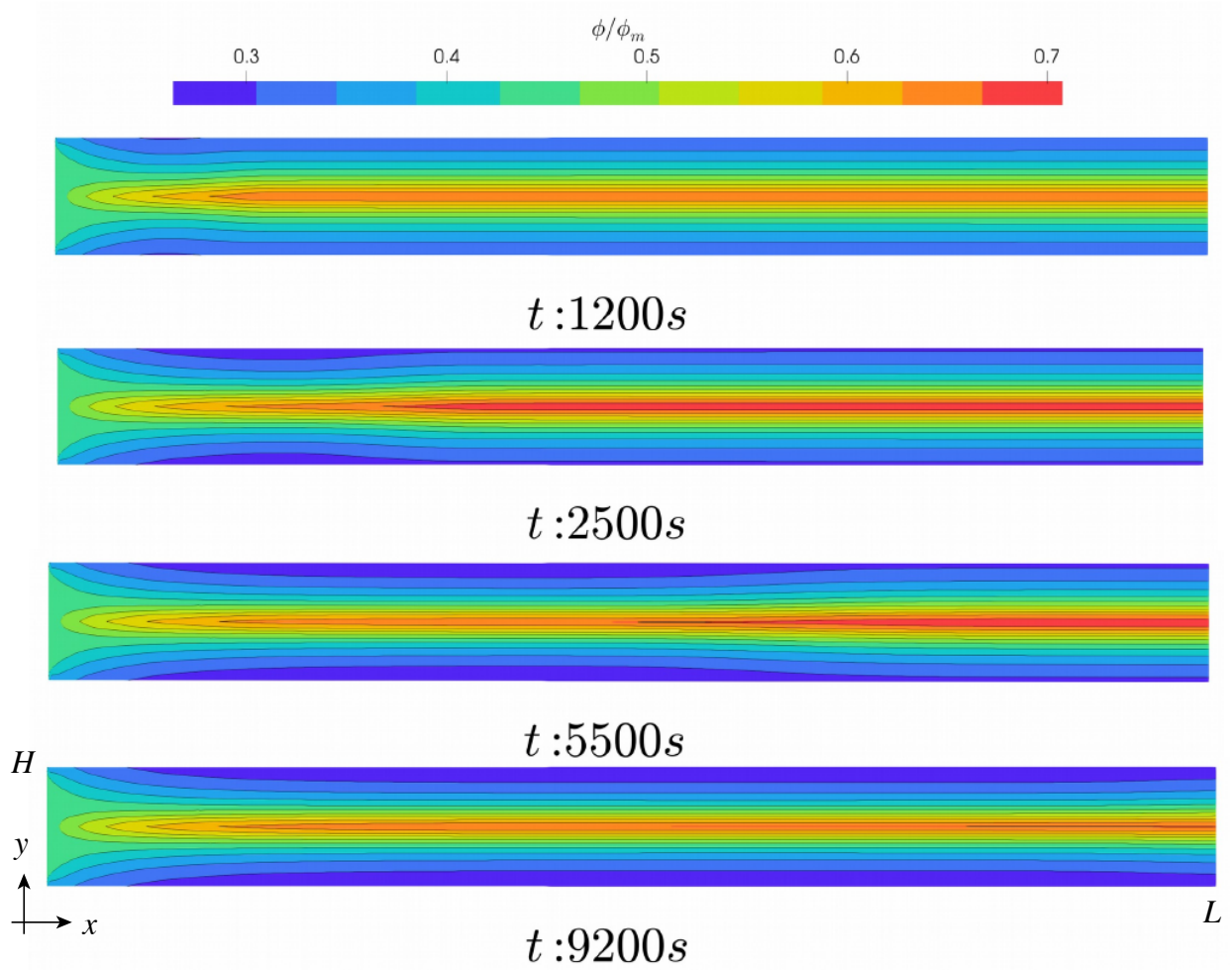


Figure 4: Time-evolution of the particle volume concentration in the “full” (non-periodic) 2D channel for $\phi_b = 0.3$. The channel has been scaled in the axial x -direction by a factor of 10^{-2} for display purposes.

which can be attributed to the inlet boundary condition. In each situation, the domain is initialized with a fixed average particle volume concentration ϕ_b , which is conserved in the case of a periodic channel. In the full channel, ϕ_b likewise correspond to the fixed particle concentration at the inlet. The latter value is not conserved along the channel. Instead, for each axial cross-section A , the average volumetric flux $\langle \mathbf{u}_p \phi \rangle_A$ is conserved. This leads to an overall over-prediction of the particle concentration in a fully periodic configuration.

The disturbance induced by the inlet boundary condition is propagated at a finite speed throughout the domain, as shown in figure 4. The time required for the inlet effects to propagate through the channel is significantly larger than the characteristic time of the particle migration process, and this should be considered when taking measurements in actual microchannels. In fact, far away from the inlet the concentration profile reaches an apparent steady state, which is analogous to our results from the fully periodic channel simulations in figure 3. Sections of the channel reached by the inlet disturbance switch from mass conservative (the area-averaged particle concentration is the same for each section) to flux conservative (the area-averaged particle concentration *flux* is the same for each section).

4.2. Suspension flow in a cylindrical Couette cell

Next, we test our TFM solver on the Couette cell geometry depicted in figure 5, where the domain consists of the region between two concentric cylinders. The inner cylinder rotates about its central axis with angular velocity ω , while the outer cylinder is fixed. The system is initialized with a uniform particle volume concentration $\phi_b = 0.5$. The

mesh consists of 20 cells in the radial direction and the closure models are detailed in table 2. This flow configuration has been studied experimentally in [47] and numerically using the SBM in [7, 39]. Additionally, a semi-analytic model was proposed by Dbouk et al. [7]. All these studies are in good agreement and predict similar concentration profiles.

closure	expression	coefficients
$f(\phi)$	equation (29)	$\alpha = 4$
$\eta_N(\phi)$	equation (27)	$K_N = 0.75$
μ_p/μ_f	equation (26)	$a_\mu = 0, b_\mu = 2.5, c_\mu = 0.1$
$\lambda_i(\phi)$	constant values	{1.0, 0.8, 0.5}
ϕ_m	constant value	0.68
$\dot{\gamma}_{NL}$	constant value	0

Table 2: Closure models and parameters used for the Couette (cylindrical) configuration.

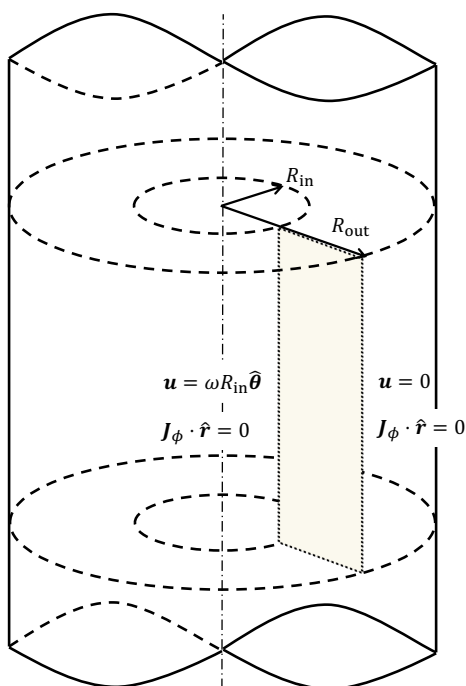


Figure 5: Schematic representation of the Couette cell geometry. The “one-dimensional” mesh corresponds to the shaded region in the radial direction between $r = R_{in}$ and $r = R_{out}$. Here, ω is the angular velocity of the inner cylinder, $\hat{\theta}$ is the unit normal vector in the azimuthal direction, and \hat{r} is the unit normal vector in the radial direction. Boundary conditions are shown for the surfaces $r = R_{in}$ and $r = R_{out}$, while an empty boundary condition is applied in the axial direction. A ‘wedge’ boundary condition is applied in the angular direction.

In the Couette cell, a homogeneous suspension fills the gap between two concentric cylinders of radii $R_{in} = 0.64$ cm and $R_{out} = 2.34$ cm. At the initial time $t = 0$ s, the inner cylinder starts spinning with angular velocity ω , thus giving rise to a shear in the radial direction, which induces particle migration. Experiments employed a suspension composed of Poly(methyl methacrylate) (PMMA) spheres with mean diameter $d_p = 675 \mu\text{m}$ suspended in a Newtonian fluid having dynamic viscosity $\mu_f = 9.45$ Pa s. The particle and fluid densities are $\rho_f = \rho_p = 1.183$ g cm⁻³. We again employed the set of parameters suggested by Morris and Boulay [39] in our rheology models. Figure 6 show that the TFM is in good agreement with results from previous studies.

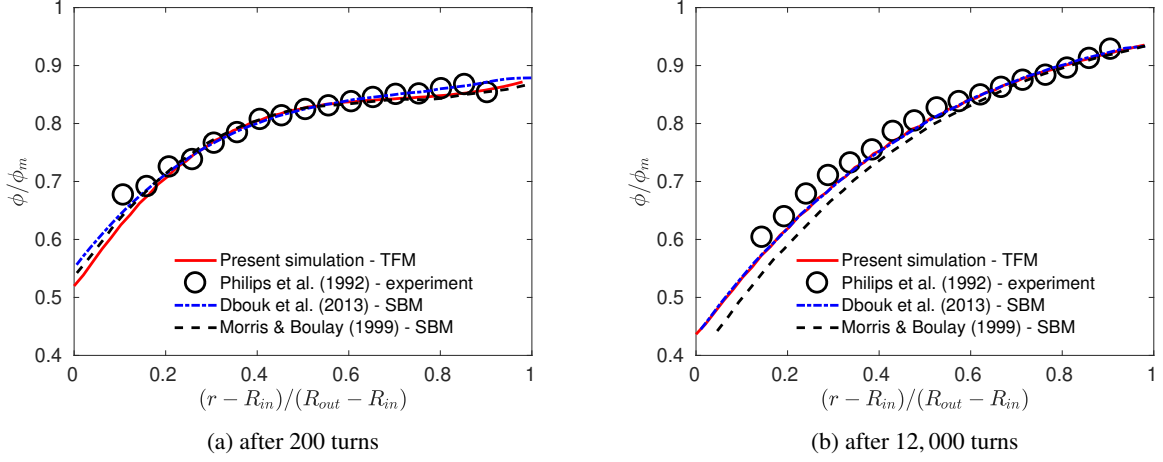


Figure 6: Comparison between the two-fluid model (TFM), the suspension balance model (SBM) and experimental data for the Couette cell geometry. No significant deviation from the expected outcomes is observed for the TFM model, thus showing good agreement.

4.3. Resuspension

Our next validation test for the TFM is in a curvilinear mixing flow with buoyancy effects, as shown schematically in figure 7. This benchmark is also an important test of the frame-invariant form of the anisotropic tensor \mathbf{Q} that we introduced in equations (24) and (25) above. This flow configuration was first employed by Abbot et al. [1] to investigate particle migration, and it has been a staple in subsequent experimental and numerical works [50, 7].

A suspension of particles with diameter $d_p = 494 \mu\text{m}$ and density $\rho_p = 1.18 \text{ g cm}^{-3}$ is suspended in a Newtonian fluid with density $\rho_f = 1.253 \text{ g cm}^{-3}$ and viscosity $\mu_f = 0.588 \text{ Pa s}$. The suspension fills the gap between two concentric cylinders of inner radius $R_{\text{in}} = 0.64 \text{ cm}$ and outer radius $R_{\text{out}} = 2.54 \text{ cm}$. The inner cylinder is set into motion by rotating it anti-clockwise, which shears the fluid, introducing a velocity gradient in the radial direction.

The fully structured mesh consists on four blocks of 50×50 cells, resulting in 50 cells in the radial direction and 200 cells in the angular direction. For time stepping, a maximum Courant number of 0.4 was imposed. This value was chosen to allow the solver to finish the *PIMPLE* loop in a flow configuration having a Courant number higher than the maximum, while still fulfilling the Courant–Friedrich–Lewy (CFL) condition [5]. In fact, the CFL condition tends to be violated near the inner cylinder when imposing a maximum Courant number close to one, as can be seen in the results of Dbouk et al. [7]. The closure models employed for this benchmark are detailed in table 3.

closure	expression	coefficients
$f(\phi)$	equation (28)	$\alpha = 4$
$\eta_N(\phi)$	equation (27)	$K_N = 0.75$
μ_p/μ_f	equation (26)	$a_\mu = -1, b_\mu = 0, c_\mu = 1$
$\lambda_i(\phi)$	equation (30)	–
ϕ_m	constant value	0.64
$\dot{\gamma}_{\text{NL}}$	constant value	0

Table 3: Closure models and parameters used in the resuspension configuration.

As shown in figure 8, our TFM implementation is able to capture a range of features in this flow, such as the formation of a thin particle layer in the mixing direction as well as the existence of a low particle density region at the bottom of the cylinder. However, we point out that the particle volume fraction distribution is strongly dependent on the choice of the closure models and the corresponding closure coefficients [7], in particular the choice of ϕ_m . This sensitivity means that model calibration is needed when simulating such complex flows. Therefore, future research should address the issue of ‘universal’ rheological closures for dense suspensions.

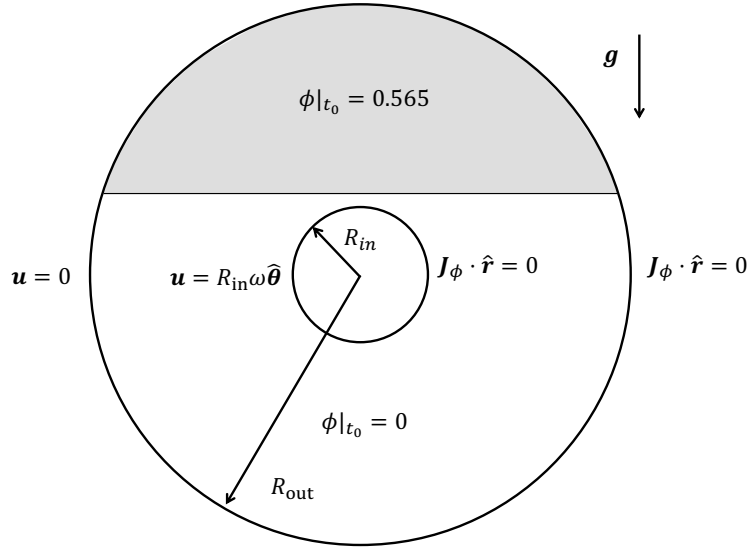


Figure 7: Schematic representation of a cylindrical mixer with rotating inner cylinder. The domain is initialized with two regions of uniform but different particle volume concentration $\phi|_{t_0}$, with clear fluid in the lower part of the mixer. The size of these regions is adjusted to obtain an average initial particle volume concentration $\phi_b = 0.2$. Here, ω is the angular velocity of the inner cylinder, and $\hat{\theta}$ is the unit normal vector in the azimuthal direction. Boundary conditions are shown for the surfaces $r = R_{in}$ and $r = R_{out}$, while an empty boundary condition is applied in the axial direction.

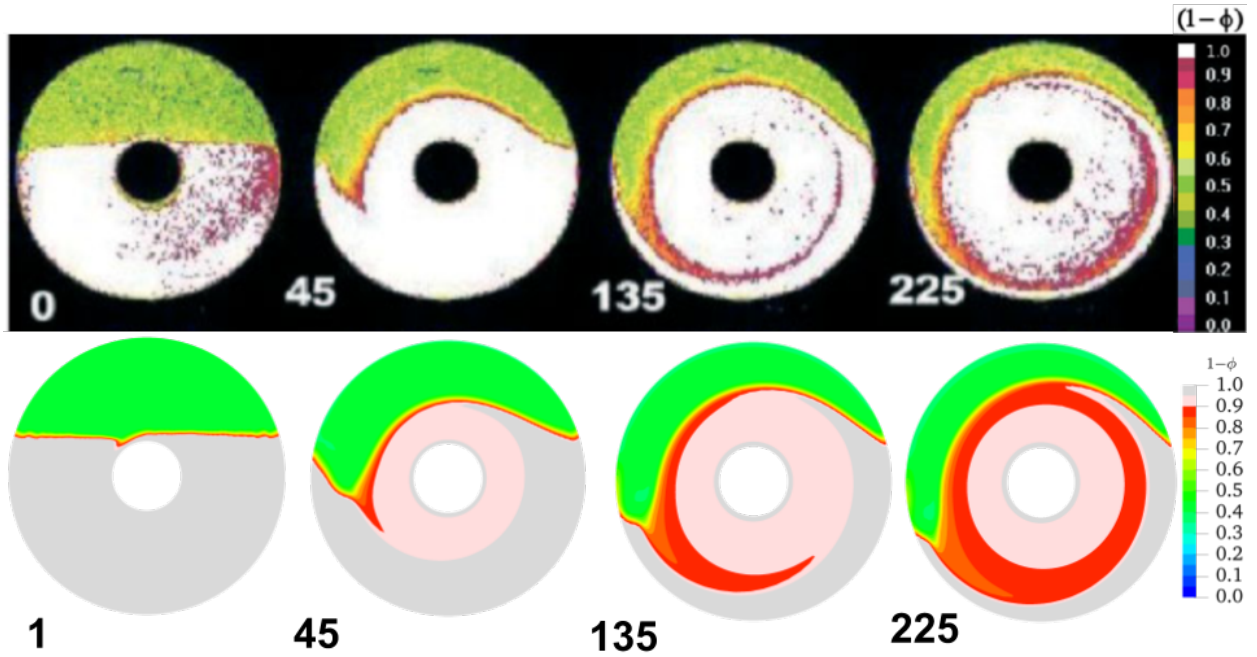


Figure 8: Comparison between our numerical TFM results (bottom) and the resuspension experiment from Rao et al. [50] (top) [Reprinted with permission from [50] ©2002 John Wiley & Sons, Ltd]. Numbers on the bottom left correspond to the number of turns of the inner cylinder.

4.4. Secondary flows: Symmetric herringbone channel

Suspension flows in channels with 2D and 3D flows features have been studied experimentally [17, 18] due to their importance for enhancing mixing and transport rates at low Reynolds numbers [44]. Specifically, symmetric herringbone channels (inspired by the so-called “staggered herringbone mixer” [57]) lead to the emergence of a

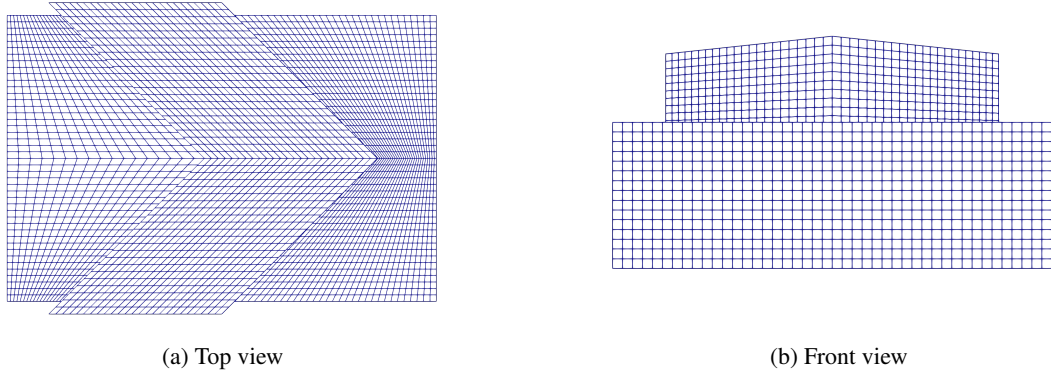


Figure 9: Computational grid employed for the simulation of secondary flows in a symmetric herringbone channel. A square channel with dimensions $135\ \mu\text{m} \times 90\ \mu\text{m} \times 30\ \mu\text{m}$ is employed and the herringbone structure is $20\ \mu\text{m}$ high and $50\ \mu\text{m}$ long.

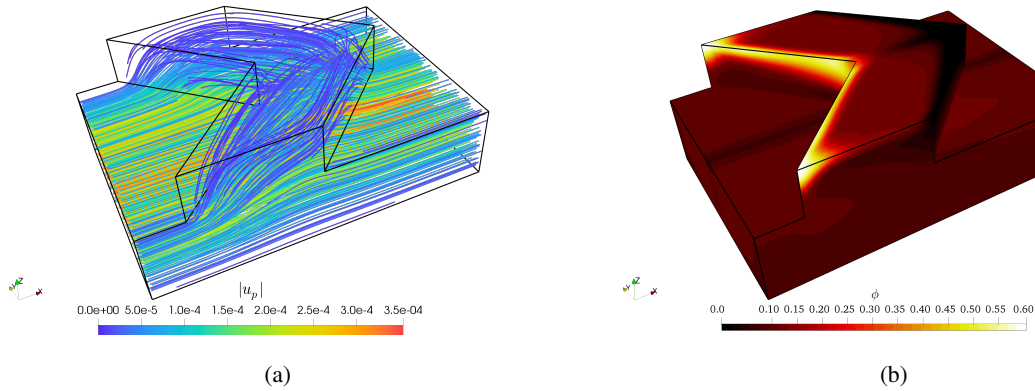


Figure 10: (a) Particle velocity streamlines and (b) particle volume concentration in the symmetric herringbone channel computed using the TFM.

vertical band of low concentration in the center of the channel, thus a particle migration flux is established towards the lateral walls. In this subsection, we simulate this phenomenon using the proposed TFM. The geometry employed is depicted in figure 9 together with the numerical grid. The geometry and material properties are chosen according to the experiment of Gao and Gilchrist [17].

We employed a fully periodic domain, and we enforced the flow rate via a forcing term in the governing equations. Additionally, we initialized the system with a uniform suspension with particle volume concentration $\phi_b = 0.1$. The choice of a fully periodic domain induces a significant difference with respect to experimental works, where a suspension was pumped in a long channel initialized with a clear fluid. In fact, not only do we expect a similar discrepancy as that discussed in section 4.1, but we also do not expect that the Kelvin–Helmoltz (KH) instability discussed in [17] would arise, as this instability is due to the shearing of the clear fluid initially filling the cavities (while we have initialized our simulations with a homogeneous suspension therein). The KH instability latter effect is responsible for the asymmetric concentration profile observed in the experiments [17].

For these simulations, we employed particles with diameter $d_p = 1.01\ \mu\text{m}$ and density $\rho_p = 2\ \text{g/cm}^3$, while the fluid has density $\rho_f = 1.2\ \text{g cm}^{-3}$ and viscosity $\mu_f = 0.04\ \text{Pa s}$. Thus, particles will tend to sink due to the density difference. The closures employed in this simulation are the same as in table 1. Due to the non-orthogonality of the mesh, multiple corrector steps are employed to obtain a stable solution.

Figure 10 shows the velocity and particle volume concentration after a steady state is reached. We observe that the particle volume concentration reaches its maximum and minimum values inside the cavity, corresponding to the most and least quiescent regions. In fact, we observed that, during the first few time steps, the particle concentration increases in the vertical direction in the channel and subsequently decreases while particles are accumulating in the

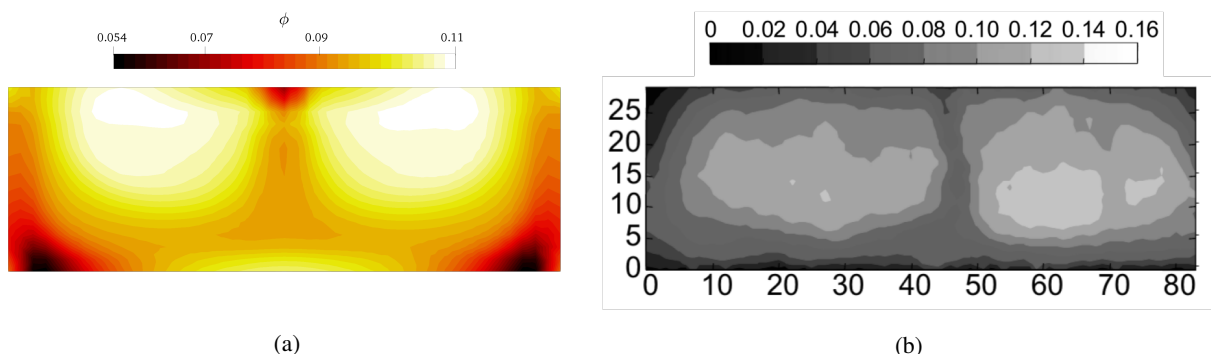


Figure 11: Comparison between (a) the TFM solver and (b) the experiment from Gao and Gilchrist [17] [Reprinted with permission from [17] ©2008 American Physical Society]. Color maps represent the particle volume concentration.

rear of the herringbone structure. This phenomenon would be less evident in experiments due to the presence of clear fluid in the cavities.

A comparison between our results and those from Gao and Gilchrist [17] is shown in figure 11. Clearly, our TFM solver is able to predict the existence of two symmetric regions separated by a vertical line of low particle concentration. Obtaining quantitative agreement through extensive model calibration is beyond the scope of this simulation, since that would also require much more faithful numerical modeling of the experimental conditions. However, this test case demonstrates that our TFM solver is able to reproduce the physics of particle migration induced by complex features in the flow geometry.

5. Conclusions

In this work, we presented a two-fluid formulation of the shear-dominated flow of a dense suspension. The proposed two-fluid model (TFM) allows us to simulate general unsteady curvilinear flows accounting for anisotropic constitutive models. The TFM was implemented as an extension of the OpenFOAM[®] *twoPhaseEulerFoam* solver, and it is thus freely available for usage and improvement by anyone. We demonstrated that the solver is capable of accurately reproducing results from experiments and previous simulations based on the (less general) suspension balance model. Furthermore, the solver can be employed to study complex curvilinear suspension flows, and it can handle various non-orthogonal geometries. Therefore, in future work, the proposed TFM could be adapted to study, for example, highly unsteady particle migration in oscillatory flows in cylindrical geometries, a topic of significant current interest [54, 6], and provide further insight into Taylor dispersion of dense suspensions [21, 49].

However, further research needs to be performed in order to develop rheological models tailored for the TFM. Specifically, models that distinguish between long-range hydrodynamic interactions [38] and contact frictional forces should be researched in order to develop a simulation tool that is capable of predicting transitions between flow regimes (for example, from non-Brownian to Brownian). Therefore, future research should perhaps be devoted to isolating the rheology of the particle phase from that of the mixture.

The OpenFOAM[®] code associated with this work can be freely downloaded from the first author's GitHub repository (<https://github.com/fmuni/twoFluidsNBSuspensionFoam>), together with the cases corresponding to the simulations performed in this work.

Acknowledgements

Acknowledgment is made to the donors of the American Chemical Society Petroleum Research Fund for support of this research under ACS PRF award # 57371-DNI9. P.P.N. additionally acknowledges the S.N. Bose Scholars program of SERB-IUSSTF for funding his internship at Purdue during Summer 2018.

Appendix A. Grid convergence analysis

In this appendix, we show that the numerical grids we employed are sufficient to capture the requisite details of the suspension flows considered. We express the degree of refinement using the number of cells h in the shear direction, which is defined as $h = H/\Delta y$ for the parallel channel and as $h = (R_{\text{out}} - R_{\text{in}})/\Delta r$ for the Couette cell.

Concerning the Poiseuille channel flow, figure A.12a shows the case of $\phi_b = 0.3$, which is the most sensitive to the grid size (since the particle volume concentration is far from the packing fraction ϕ_m). We remark that using different expressions for the non-local shear rate $\dot{\gamma}_{\text{NL}}$ leads to different grid dependencies, since the non-local shear rate is meant to limit the particle volume concentration at the centerline of the channel.

Similarly, figure A.12b shows that, in the case of the Couette cell flow, no significant dependence on the grid size is observed for grids finer than $h = 20$. A non-local shear rate was not employed in this case.

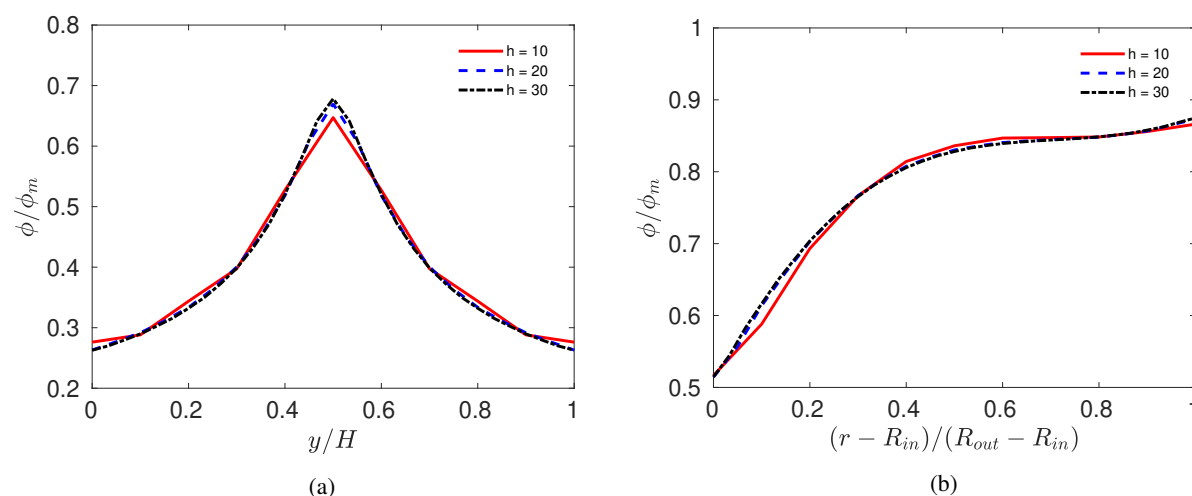


Figure A.12: Particle volume concentration profiles obtained using different grid resolutions for (a) the Poiseuille channel flow ($\phi_b = 0.3$) and (b) the Couette cell flow (200 turns of the inner cylinder).

References

- [1] J. R. Abbott, N. Tetlow, A. L. Graham, S. A. Altobelli, E. Fukushima, L. A. Mondy, T. S. Stephens, Experimental observations of particle migration in concentrated suspensions: Couette flow, *J. Rheol.* 35 (1991) 773–795. doi:10.1122/1.550157.
- [2] J. P. Boris, D. L. Book, Flux-corrected transport, *J. Comput. Phys.* 135 (1997) 172–186. doi:10.1006/jcph.1997.5700.
- [3] F. Boyer, E. Guazzelli, O. Pouliquen, Unifying suspension and granular rheology, *Phys. Rev. Lett.* 107 (2011) 188301. doi:10.1103/PhysRevLett.107.188301.
- [4] C. E. Brennen, *Fundamentals of Multiphase Flow*, Cambridge University Press, Cambridge, 2005. doi:10.1017/CB09780511807169. URL <http://ebooks.cambridge.org/ref/id/CB09780511807169>
- [5] R. Courant, H. Lewy, K. Friedrichs, Über die partiellen Differenzgleichungen der mathematischen Physik, *Math. Ann.* 100 (1928) 32–74. doi:10.1007/BF01448839.
- [6] F. R. Cui, A. A. Howard, M. R. Maxey, A. Tripathi, Dispersion of a suspension plug in oscillatory pressure-driven flow, *Phys. Rev. Fluids* 2 (2017) 094303. doi:10.1103/PhysRevFluids.2.094303.
- [7] T. Dbouk, E. Lemaire, L. Lobry, F. Moukalled, Shear-induced particle migration: Predictions from experimental evaluation of the particle stress tensor, *J. Non-Newtonian Fluid Mech.* 198 (2013) 78–95. doi:10.1016/j.jnnfm.2013.03.006.
- [8] T. Dbouk, L. Lobry, E. Lemaire, Normal stresses in concentrated non-Brownian suspensions, *J. Fluid Mech.* 715 (2013) 239–272. doi:10.1017/jfm.2012.516.
- [9] M. M. Denn, J. F. Morris, Rheology of non-Brownian suspensions, *Ann. Rev. Chem. Biomolec. Eng.* 5 (2014) 203–228. doi:10.1146/annurev-chembioeng-060713-040221.
- [10] H. J. Di, K. C. Cameron, Reducing environmental impacts of agriculture by using a fine particle suspension nitrification inhibitor to decrease nitrate leaching from grazed pastures, *Agric. Ecosyst. Environ.* 109 (2005) 202–212. doi:10.1016/J.AGEE.2005.03.006.
- [11] R. Di Felice, Hydrodynamics of liquid fluidisation, *Chem. Eng. Sci.* 50 (1995) 1213–1245. doi:10.1016/0009-2509(95)98838-6.
- [12] E. V. Dontsov, A. P. Peirce, Slurry flow, gravitational settling and a proppant transport model for hydraulic fractures, *J. Fluid Mech.* 760 (2014) 567–590. doi:10.1017/jfm.2014.606.

- [13] E. V. Dontsov, A. P. Peirce, Proppant transport in hydraulic fracturing: Crack tip screen-out in KGD and P3D models, *Int. J. Solids Structs* 63 (2015) 206–218. doi:10.1016/j.ijsolstr.2015.02.051.
- [14] I. Drijer, T. van de Laar, H. M. Vollebregt, C. Schroën, From highly specialised to generally available modelling of shear induced particle migration for flow segregation based separation technology, *Sep. Purif. Technol.* 192 (2018) 99–109. doi:10.1016/j.seppur.2017.10.001.
- [15] J. H. Ferziger, M. Perić, Solution of the Navier-Stokes Equations, in: *Computational Methods for Fluid Dynamics*, Springer, Berlin/Heidelberg, 2002, pp. 157–216. doi:10.1007/978-3-642-56026-2_{_}7.
- [16] Y. Forterre, O. Pouliquen, Flows of dense granular media, *Annu. Rev. Fluid Mech.* 40 (2008) 1–24. doi:10.1146/annurev.fluid.40.111406.102142.
- [17] C. Gao, J. F. Gilchrist, Shear-induced particle migration in one-, two-, and three-dimensional flows, *Phys. Rev. E* 77 (2008) 025301. doi:10.1103/PhysRevE.77.025301.
- [18] C. Gao, B. Xu, J. F. Gilchrist, Mixing and segregation of microspheres in microchannel flows of mono- and bidispersed suspensions, *Phys. Rev. E* 79 (2009) 36311. doi:10.1103/PhysRevE.79.036311.
- [19] D. Gidaspow, *Multiphase Flow and Fluidization: Continuum and Kinetic Theory Descriptions*, Academic Press, San Diego, CA, 1994.
- [20] I. Goldhirsch, Introduction to granular temperature, *Powder Technol.* 182 (2008) 130–136. doi:10.1016/J.POWTEC.2007.12.002.
- [21] I. M. Griffiths, H. A. Stone, Axial dispersion via shear-enhanced diffusion in colloidal suspensions, *EPL* 97 (2012) 58005. doi:10.1209/0295-5075/97/58005.
- [22] E. Guazzelli, O. Pouliquen, Rheology of dense granular suspensions, *J. Fluid Mech.* 852 (2018) P1. doi:10.1017/jfm.2018.548.
- [23] M. Han, C. Kim, M. Kim, S. Lee, Particle migration in tube flow of suspensions, *J. Rheol.* 43 (1999) 1157–1174. doi:10.1122/1.551019.
- [24] J. D. Hymann, J. Jiménez-Martínez, H. S. Viswanathan, J. W. Carey, M. L. Porter, E. Rougier, S. Karra, Q. Kang, L. Frash, L. Chen, Z. Lei, D. O'Malley, N. Makedonska, Understanding hydraulic fracturing: a multi-scale problem, *Phil. Trans. R. Soc. A* 374 (2016) 20150426. doi:10.1098/rsta.2015.0426.
- [25] L. Isa, R. Besseling, W. C. K. Poon, Shear zones and wall slip in the capillary flow of concentrated colloidal suspensions, *Phys. Rev. Lett.* 98 (2007) 198305. doi:10.1103/PhysRevLett.98.198305.
- [26] R. Jackson, Locally averaged equations of motion for a mixture of identical spherical particles and a Newtonian fluid, *Chem. Eng. Sci.* 52 (1997) 2457–2469. doi:10.1016/S0009-2509(97)00065-1.
- [27] P. Jop, Y. Forterre, O. Pouliquen, A constitutive law for dense granular flows, *Nature* 441 (2006) 727–730. doi:10.1038/nature04801.
- [28] C. J. Koh, P. Hookham, L. G. Leal, An experimental investigation of concentrated suspension flows in a rectangular channel, *J. Fluid Mech.* 266 (1994) 1–32. doi:10.1017/S0022112094000911.
- [29] D. Leighton, A. Acrivos, The shear-induced migration of particles in concentrated suspensions, *J. Fluid Mech.* 181 (1987) 415–439. doi:10.1017/S0022112087002155.
- [30] C. K. K. Lun, S. B. Savage, The effects of an impact velocity dependent coefficient of restitution on stresses developed by sheared granular materials, *Acta Mech.* 63 (1986) 15–44. doi:10.1007/BF01182538.
- [31] M. K. Lyon, L. G. Leal, An experimental study of the motion of concentrated suspensions in two-dimensional channel flow. Part 1. Monodisperse systems, *J. Fluid Mech.* 363 (1998) 25–56. doi:10.1017/S0022112098008817.
- [32] S. H. Maron, A. W. Sisko, Application of Ree-Eyring generalized flow theory to suspensions of spherical particles, *J. Colloid Sci.* 12 (1957) 99–107. doi:10.1016/0095-8522(57)90031-4.
- [33] M. Maxey, Simulation methods for particulate flows and concentrated suspensions, *Annu. Rev. Fluid Mech.* 49 (2017) 171–193. doi:10.1146/annurev-fluid-122414-034408.
- [34] C. C. Milioli, F. E. Milioli, W. Holloway, K. Agrawal, S. Sundaresan, Filtered Two-Fluid Models of Fluidized Gas-Particle Flows: New Constitutive Relations, *AIChE J.* 59 (2013) 3265–3275. doi:10.1002/aic.
- [35] R. M. Miller, J. F. Morris, Normal stress-driven migration and axial development in pressure-driven flow of concentrated suspensions, *J. Non-Newtonian Fluid Mech.* 135 (2006) 149–165. doi:10.1016/J.JNNFM.2005.11.009.
- [36] P. Mills, P. Snabre, Rheology and structure of concentrated suspensions of hard spheres. Shear induced particle migration, *J. Physique II* 5 (1995) 1597–1608. doi:10.1051/jp2:1995201.
- [37] P. Mirbod, Two-dimensional computational fluid dynamical investigation of particle migration in rotating eccentric cylinders using suspension balance model, *Int. J. Multiphase Flow* 80 (2016) 79–88. doi:10.1016/j.ijmultiphaseflow.2015.11.002.
- [38] J. F. Morris, Lubricated-to-frictional shear thickening scenario in dense suspensions, *Phys. Rev. Fluids* 3 (2018) 110508. doi:10.1103/PhysRevFluids.3.110508.
- [39] J. F. Morris, F. Boulay, Curvilinear flows of noncolloidal suspensions: The role of normal stresses, *J. Rheol.* 43 (1999) 1213–1237. doi:10.1122/1.551021.
- [40] J. F. Morris, J. F. Brady, Pressure-driven flow of a suspension: Buoyancy effects, *Int. J. Multiphase Flow* 24 (1998) 105–130. doi:10.1016/S0301-9322(97)00035-9.
- [41] F. Moukalled, L. Mangani, M. Darwish, *The Finite Volume Method in Computational Fluid Dynamics: An Advanced Introduction with OpenFOAM® and Matlab*, Fluid Mechanics and its Applications, Springer International Publishing, Cham, Switzerland, 2016. doi:10.1007/978-3-319-16874-6.
- [42] P. R. Nott, J. F. Brady, Pressure-driven flow of suspensions: simulation and theory, *J. Fluid Mech.* 275 (1994) 157–199. doi:10.1017/S0022112094002326.
- [43] P. R. Nott, E. Guazzelli, O. Pouliquen, The suspension balance model revisited, *Phys. Fluids* 23 (2011) 043304. doi:10.1063/1.3570921.
- [44] J. M. Ottino, S. Wiggins, Introduction: mixing in microfluidics, *Phil. Trans. R. Soc. Lond. A* 362 (2004) 923–935. doi:10.1098/rsta.2003.1355.
- [45] A. Passalacqua, R. O. Fox, Implementation of an iterative solution procedure for multi-fluid gas-particle flow models on unstructured grids, *Powder Technol.* 213 (2011) 174–187. doi:10.1016/j.powtec.2011.07.030.
- [46] P. Pham, B. Metzger, J. E. Butler, Particle dispersion in sheared suspensions: Crucial role of solid-solid contacts, *Phys. Fluids* 27 (2015) 051701. doi:10.1063/1.4919728.

- [47] R. J. Phillips, R. C. Armstrong, R. A. Brown, A. L. Graham, J. R. Abbott, A constitutive equation for concentrated suspensions that accounts for shear-induced particle migration, *Phys. Fluids A* 4 (1992) 30–40. doi:10.1063/1.858498.
- [48] F. Picano, W.-P. Breugem, D. Mitra, L. Brandt, Shear thickening in non-Brownian suspensions: An excluded volume effect, *Phys. Rev. Lett.* 111 (2013) 098302. doi:10.1103/PhysRevLett.111.098302.
- [49] A. Ramachandran, A macrotransport equation for the particle distribution in the flow of a concentrated, non-colloidal suspension through a circular tube, *J. Fluid Mech.* 734 (2013) 219–252. doi:10.1017/jfm.2013.455.
- [50] R. Rao, L. Mondy, A. Sun, S. Altobelli, A numerical and experimental study of batch sedimentation and viscous resuspension, *Int. J. Numer. Meth. Fluids* 39 (2002) 465–483. doi:10.1002/flid.246.
- [51] G. Segré, A. Silberberg, Radial particle displacements in Poiseuille flow of suspensions, *Nature* 189 (1961) 209–210. doi:10.1038/189209a0.
- [52] D. Semwogerere, J. F. Morris, E. R. Weeks, Development of particle migration in pressure-driven flow of a Brownian suspension, *J. Fluid Mech.* 581 (2007) 437–451. doi:10.1017/S0022112007006088.
- [53] S. Shiozawa, M. McClure, Simulation of proppant transport with gravitational settling and fracture closure in a three-dimensional hydraulic fracturing simulator, *J. Petrol. Sci. Eng.* 138 (2016) 298–314. doi:10.1016/j.petrol.2016.01.002.
- [54] B. Snook, J. E. Butler, E. Guazzelli, Dynamics of shear-induced migration of spherical particles in oscillatory pipe flow, *J. Fluid Mech.* 786 (2016) 128–153. doi:10.1017/jfm.2015.645.
- [55] J. J. Stickel, R. L. Powell, Fluid mechanics and rheology of dense suspensions, *Ann. Rev. Fluid Mech.* 37 (2005) 129–149. doi:10.1146/annurev.fluid.36.050802.122132.
- [56] H. Strathmann, Membrane separation processes: Current relevance and future opportunities, *AIChE J.* 47 (2001) 1077–1087. doi:10.1002/aic.690470514.
- [57] A. D. Stroock, Chaotic mixer for microchannels, *Science* 295 (2002) 647–651. doi:10.1126/science.1066238.
- [58] L. Thomas, H. Tang, D. M. Kalyon, S. Aktas, J. D. Arthur, J. Blotvogel, J. W. Carey, A. Filshill, P. Fu, G. Hsuan, T. Hu, D. Soeder, S. Shah, R. Vidic, M. H. Young, Toward better hydraulic fracturing fluids and their application in energy production: A review of sustainable technologies and reduction of potential environmental impacts, *J. Petrol. Sci. Eng.* 173 (2019) 793–803. doi:10.1016/j.petrol.2018.09.056.
- [59] P. Valkó, M. J. Economides, *Hydraulic Fracture Mechanics*, John Wiley & Sons, New York, NY, 1995.
- [60] H. M. Vollebregt, R. G. M. van der Sman, R. M. Boom, Suspension flow modelling in particle migration and microfiltration, *Soft Matter* 6 (2010) 6052–6064. doi:10.1039/c0sm00217h.
- [61] H. G. Weller, G. Tabor, C. Fureby, H. Jasak, A tensorial approach to computational continuum mechanics using object-oriented techniques, *Comput. Phys.* 12 (1998) 620–631. doi:10.1063/1.168744.
- [62] K. Yeo, M. R. Maxey, Dynamics and rheology of concentrated, finite-Reynolds-number suspensions in a homogeneous shear flow, *Phys. Fluids* 25 (2013) 053303. doi:10.1063/1.4802844.
- [63] K. Yeo, M. Maxey, Numerical simulations of concentrated suspensions of monodisperse particles in a Poiseuille flow, *J. Fluid Mech.* 682 (2011) 491–518. doi:10.1017/jfm.2011.241.
- [64] S. T. Zalesak, Fully multidimensional flux-corrected transport algorithms for fluids, *J. Comput. Phys.* 31 (1979) 335–362. doi:10.1016/0021-9991(79)90051-2.